



Air spreading through wetted cellulose membranes: Implications for the safety function of hydraulic valves in plants

JooYoung Park, Taesik Go, Jeongeun Ryu, and Sang Joon Lee *

Department of Mechanical Engineering, Pohang University of Science and Technology, San 31, Hyoja-dong, Pohang 37673, South Korea

 (Received 29 April 2019; published 19 September 2019)

Plants transport water against the risk of cavitation inside xylem vessels, called “embolism.” As one of their hydraulic strategies, pit membranes composed of cellulose fibers have been known as safety valves that prevent the spreading of embolism towards adjacent xylem vessels. However, detailed observation of embolism spreading through a pit membrane is still lacking. Here, we hypothesized that the pit membranes normally remain to be wetted in xylem vessels and noticed in particular the hydraulic role of water film on air spreading that has been overlooked previously. For the hydrodynamic study of the embolism spreading through a wetted pit membrane, we investigated the penetration and spreading dynamics of air plugs through the wetted cellulose membrane in a channel flow. Air spreading exhibits two types of dynamics: continuous and discrete spreading. We elucidated the correlation of dynamic characteristics of air flow and pressure variations according to membrane thickness. Our study speculates that the thickness of pit membranes affects the behaviors of water film captured by cellulose fibers, and it is a crucial criterion for the reversible gating of further spreading of embolism throughout xylem networks.

DOI: [10.1103/PhysRevE.100.032409](https://doi.org/10.1103/PhysRevE.100.032409)

I. INTRODUCTION

Plants transport water from their roots to leaves through xylem vessels by generating highly negative pressure around -2 MPa by leaf transpiration [1]. Water uptake by the suction force induces a thermodynamically unstable state causing cavitation. Bubbles formed in the vessels obstruct efficient water transport and reduce hydraulic conductivity up to 84% by expanding along the xylem channels and breaking continuous water column [2,3]. This phenomenon, which is called “embolism,” is detrimental to the growth and reproduction of vascular plants. Nevertheless, plants have evolved their structural strategies to sustain stable water transport against the risk of cavitation.

Xylem conduits are interconnected by pit membranes located at their side walls. Pit membranes have been known to work as safety valves that prevent embolism spreading to the adjacent xylem conduits, while providing alternative passages to make sap flow bypass the embolized xylem vessels [4,5]. The thickness and pore size of the pit membrane are in the range of 10^{-2} – 10^2 μm and 10^1 – 10^2 nm, respectively [6,7]. Figure 1(a) shows a scanning electron microscopic (SEM) image of pit membranes of *Acer palmatum*, which have homogeneous pit membranes woven with randomly oriented microfibrils [inset of Fig. 1(a)].

Pit membranes are mainly composed of cellulose, which is an essential structural component of plants [6,8]. Cellulose can form extensive hydrogen bonds with their abundant hydroxyl groups having high reactivity [9]. This molecular structure of cellulose contributes to its strong hydrophilicity. The cellulose microfibrils of pit membranes are also coated

with pectin, which is known as a kind of hydrophilic hydrogel [10,11]. Therefore, contact angle between the air-water meniscus and pit membrane has been assumed to be 0° indicating complete wetting [6,8,11–14].

The hydraulic roles of pit membranes to prevent the entry of embolism and its spreading have been studied with various approaches. Embolism can spread to the adjacent conduit when air bubbles seed from the embolized conduit [15]. The pressure difference that pit membranes can withstand air penetration is called “air seeding pressure.” It is an important parameter for understanding the gas sealing ability of intervessel pit membranes. Air seeding pressure has been directly measured with stems or branches by experimental methods such as centrifuge method, air dehydration, and air injection [3]. The effects of structural parameters, such as porosity [6,7], thickness [12], and morphological irregularity of pit membranes [13], on the air seeding pressure have been investigated with the aid of transmission electron microscopy and SEM. When the pressure difference exceeds the air seeding pressure, the air flow rate through pit membranes has been modelled in consideration of the deformation of pit membranes [14]. The effects of the mechanical deflection of pit membranes on the vulnerability of cavitation have been theoretically examined on the basis of the morphological structures of pits, such as pit aperture, depth of pit chamber, and membrane thickness [15,16]. However, most previous studies have been conducted by direct measurement of air seeding pressure, image analysis, and physical modeling. Therefore, the detailed hydrodynamics of the embolism spreading at a pit level, such as behaviors of air-water meniscus and variation in pressure difference across pit membranes in particular, has not been observed so far and remains unclear.

In this study, we systematically investigated the hydrodynamic characteristics of air blocking and spreading through

*sjlee@postech.ac.kr.

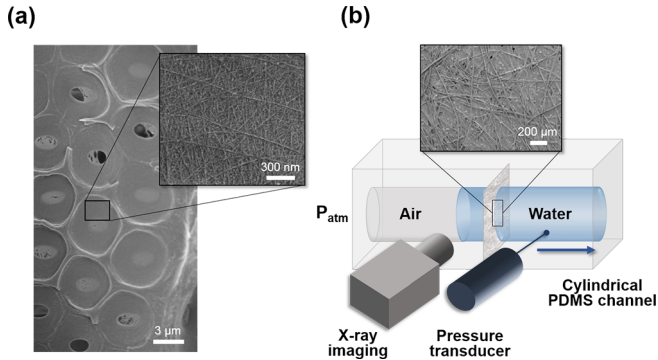


FIG. 1. Fibrous structure of pit membranes and the experimental set-up. (a) SEM image of pit membranes in xylem vessels (*Acer palmatum*). Inset shows the fibrous structure of a pit membrane. (b) Schematic of the experimental set-up. Air and water were drawn by a syringe pump and dynamic behaviors of air-water meniscus penetrating the cellulose membrane were observed by using x-ray microimaging technique. Pressure difference across the membrane was measured with a pressure transducer located at the downstream of the membrane. Inset shows SEM image of the cellulose membrane consisting of microfibers.

wetted homogeneous pit membranes by utilizing a biomimetic model system. The model system comprises a circular channel embedding cellulose membrane having different thickness. The penetration and spreading of air through the membrane was observed by using x-ray imaging technique. The temporal variations of pressure difference across the membrane were monitored with a pressure transducer. The movements of air-water meniscus and pressure variations around the wetted membrane were elucidated by correlating with dynamic behaviors of water film captured by cellulose fibers of the membrane with varying thickness of the membrane. Mechanism of the air spreading through wetted cellulose membrane provides insights for understanding the hydraulic functions of pit membranes retaining water film to limit spreading of embolism.

II. EXPERIMENTS

A. Fabrication of the pit membrane system

A model system inspired by pit membranes was fabricated for the systematic study on air blocking and seeding phenomena [Fig. 1(b)]. The fabrication process of the pit membrane model system is similar with that of our previous study [17]. An open circular channel with an inner diameter of $d = 1.5$ mm was prepared by using a Tygon tube as a channel mold [18]. A piece of cellulose membrane was inserted between two excised sections of a PDMS channel.

Korean traditional papers (Ongoeul Hanji, South Korea) made from *Broussonetia kazinoki* fibers were used as cellulose membranes for a biomimetic model of pit membranes. Four kinds of cellulose membranes in dry state (membranes A, B, C, and D) have different basis weight (mass per unit area), thickness, and two-dimensional porosity (Table I). The thickness and porosity have a negative relationship, which shows the morphological feature of cellulose membranes. The thickness of each membrane was directly measured from

TABLE I. Specifications of the cellulose membranes tested in this study.

Membrane	Basis weight (g/m^2)	Thickness (μm)	Porosity (%)
A	10.0	28.0	44.1
B	16.0	43.9	36.5
C	19.6	56.6	30.9
D	39.1	73.1	24.4

cross-sectional image of the membrane. The two-dimensional porosity of each membrane was evaluated from x-ray image of the membrane fibers stacked in depth. Membrane fibers were classified from their x-ray image. The captured x-ray image was converted into a binary image with the aid of ImageJ software. The membrane porosity was evaluated by calculating the area ratio of membrane fibers [19,20]. The inset of Fig. 1(b) shows a representative SEM image of membrane B composed of cellulose fibers. As shown in the SEM images of the membranes, numerous cellulose fibers are stacked in a thick membrane (Fig. S1) [21]. The hydrophilicity of the cellulose membranes can be verified by observing the water droplet absorbed by the dry membrane with spreading motion and decreasing contact angle (Fig. S2) [21]. The infrared spectrum of each membrane was obtained with a Fourier transform infrared spectrometer (Spectrum Two, PerkinElmer). The spectra show the band characteristics of the cellulosic polymers indicating the stretching of O–H, C–H, C–O, and wagging of CH_2 (Fig. S3) [21–24].

B. Experimental set-up

The experimental set-up of this study is similar with that of our previous study [17]. A PDMS channel embedding a cellulose membrane was filled with water to make the membrane wet. The cellulose paper was reported to be fully swelled in about 60 s [25]. In this study, experiments were conducted after the structural change due to swelling of the cellulose membrane was sufficiently saturated. Air and water inside the channel were drawn by a syringe pump (PHD 2000 and PHD Ultra, Harvard Apparatus) with a flow rate of $1 \mu\text{l}/\text{min}$. The syringe contained 0.1 ml of air for simultaneous variations of the flow and internal pressure inside the channel. Reynolds number ($\text{Re} = \rho v d / \mu$) and capillary number ($\text{Ca} = \mu v / \gamma$) were adjusted to be less than 1, in consideration of dynamic similarity with the real sap flows [1]. Effects of viscosity and surface tension are important in this flow condition. Here, ρ , μ , and γ denote the density, viscosity, and surface tension of the water, respectively. The velocity of channel flow is expressed as v .

The leakage of air bubbles through the membrane and the movement of air–water meniscus along the channel were observed by x-ray microimaging technique at the 6C Biomedical Imaging Beamline of Pohang Accelerator Laboratory (PAL, Pohang, Korea). Phase-contrast x-ray imaging method is useful to clearly visualize the dynamic behaviors of meniscus between gas and liquid. The x-ray beam of 20 keV was used and the sample-to-detector distance was fixed at 94 mm. X-ray images were consecutively captured at a frame rate of 5–10 fps with a Zyla camera (Andor Zyla, Ireland) with a

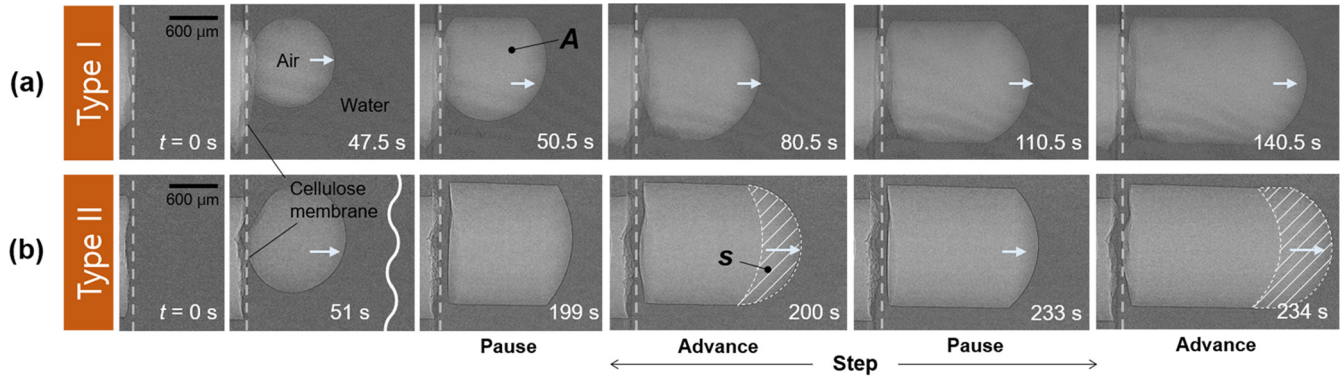


FIG. 2. Two different dynamics of air spreading throughout the channel after passing through the cellulose membrane A. (a) In the case of type I, the air continuously spreads toward downstream across the membrane marked with a dashed line. (b) In the case of type II, the air/water meniscus moves forward with repeating the advance and pause, called as “step” in this study. Step size (s) indicates the hatched area which represents the increment of air area A during a single step. Water film is formed and remains at the membrane even after the air penetrates the membrane.

4 \times objective lens. Temporal variation of the two-dimensional area of the spreading air was analyzed with ImageJ software [19]. During the air penetration process through the cellulose membrane, pressure variation at the downstream of the membrane was monitored with a pressure transducer (PX409-015GUSB, Omega engineering). The opposite end of the channel was opened to the atmospheric pressure (P_{atm}).

III. RESULTS

The sequential x-ray images in Fig. 2 demonstrate the representative dynamic behaviors of air blocking and spreading across membrane A. Air and water appear as the bright and dark regions, respectively. They move from the left to the right side of the channel. The air-water meniscus meets the membrane at $t = 0$. The movement of the air is sealed by the membrane for approximately 50 s. Then, the air starts to pass through the membrane, forms an air bubble, and spreads along the channel. Even after the air bubble grows into air plug, water film remains near the membrane.

The air spreading across the cellulose membrane exhibits two distinctive dynamics. The continuous air spreading was designated as “type I” and the discrete air spreading as “type II,” as shown in Figs. 2(a) and 2(b), respectively. Type I of air spreading, which is similar with our previous result [17], was only observed when the air–water meniscus passed through the thinnest membrane A. Meanwhile, type II of air spreading was observed in all membranes tested in this study. For the case of type I, the meniscus gradually advances to the right side of the channel. However, it discretely spreads along the channel by repeating the advance and the pause in the case of type II. Here, a cycle of the rapid advance and pause was called as a “step.” For the quantification of the positional variation of the air-water meniscus, temporal variation of air area A was evaluated from the x-ray images. The increment of air area A during a single step, which is represented by a hatched region of crescent shape [Fig. 2(b)], indicates the step size s .

Figure 3(a) shows that the temporal variations of the air area A increase as the air spreads along the channel. Filled circles and the other hollow symbols indicate the continuous spreading (type I) and the discontinuous spreading (type II),

respectively. Until the meniscus reaches the membrane ($t < 0$), the area A gradually increases. As the meniscus contacts the membrane at $t = 0$, it stops at the membrane. Then the area A is maintained in a nearly constant manner. Afterwards, the air starts to penetrate through the membrane. Then, it rapidly spreads across the membrane with a sudden increase of A at the moment marked with filled diamonds. For a thick membrane, air takes a long time to pass through the membrane. In type I, air area A gradually increases due to the continuous air penetration across the membrane A. By contrast, in type II, air leaks in the form of air bubbles that are snapped off from the membrane. They coalesce into an air plug in the downstream of the channel. As air spreads along the channel while repeating the steps of stop and advance, the area A increases discretely as shown in Fig. 3(a). The meniscus passing through a thick membrane exhibits frequent occurrence of the stop and advance. In other words, the step size s and the period of steps decrease as the thickness of the membrane increases. Dynamic behavior of the air spreading across each membrane is provided in Fig. S4 and Videos S1–S5 [21].

Figure 3(b) shows temporal variations of the ensemble averages of negative pressure P measured at the downstream of the membrane during air penetration through each membrane and spreading along the channel. The standard deviation of each graph is represented as shaded area. The pressure remains close to the atmospheric pressure before the meniscus meets the membrane ($t < 0$). When the meniscus reaches the membrane ($t = 0$), P starts to decrease gradually. Pressure continuously decreases when the meniscus stays at the membrane. Air begins to pass through the membrane when P reaches the threshold pressure P_{th} , as indicated by filled diamond symbols. Pressure gets to the level of P_{th} in the order of thickness of the membrane. In type I, P rapidly increases to the level of atmospheric pressure after it reaches P_{th} . However, in type II, pressure is maintained at a negative value lower than the atmospheric pressure; it repeatedly fluctuates with an amplitude ΔP_s . Pressure fluctuates with low amplitude ΔP_s as the air spreads across a thick membrane.

Pressure variation in the type II was further analyzed from the result of Fig. 3(b). Figure 4(a) compares the absolute

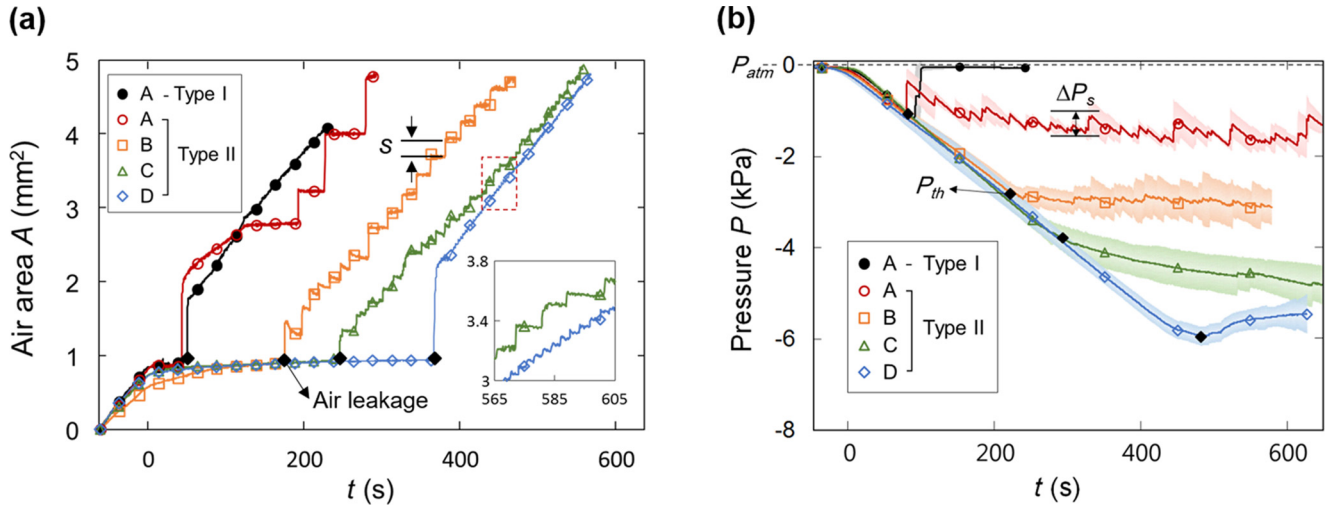


FIG. 3. Hydrodynamic characteristics of the air spreading across the membranes with different thicknesses. (a) Temporal variations of the air area A . Inset shows the magnified view of the region indicated by a red-dashed rectangle. (b) Temporal variations of the pressure measured at the downstream of each membrane. The threshold pressure when the air begins to pass through the membrane and the amplitude of pressure fluctuations during the air spreading are denoted as P_{th} and ΔP_s , respectively. The standard deviation of each graph is represented as shaded area.

values of P_{th} according to the membrane, when the air starts to spread across the membranes. As the thickness of the membrane increases from membrane A to membrane D, the absolute value $|P_{th}|$ increases as 1.16 ± 0.19 , 2.95 ± 0.40 , 3.72 ± 0.82 , and 6.45 ± 0.73 kPa, in membranes A, B, C, and D, respectively. Pressure variation during the air spreading process was examined by using fast Fourier transform (FFT) to examine the distribution of the amplitude ΔP_s according to the frequency f of pressure fluctuations [Fig. 4(b)]. Sixty points were selected in the order of larger amplitude from the FFT results. Solid lines represent the fitting curves of each experimental condition in a form of exponential function. As the membrane thickness increases, pressure fluctuations ΔP_s decrease and the frequency f is distributed in a broad region.

IV. DISCUSSION

A. Blockage of air spreading by the wetted cellulose membrane

Figure 5 illustrates the detailed air spreading process through a membrane pore in a microscopic view. As the air–water meniscus is pulled against the membrane (Fig. 5(a), Fig. S5, and videos S6 and S7 [21]), pressure P at the water side keeps decreasing [Fig. 3(b)]. Air penetration is blocked by the wetted membrane pores, because the hydrophilic cellulose membrane retains water in its pores. When pressure reaches the threshold pressure P_{th} , the air bubble leaks from the largest pore by forming an air passage through the overlapped cellulose fibers covered with water [Fig. 5(b)]. The threshold pressure $|P_{th}|$ is determined by Laplace pressure

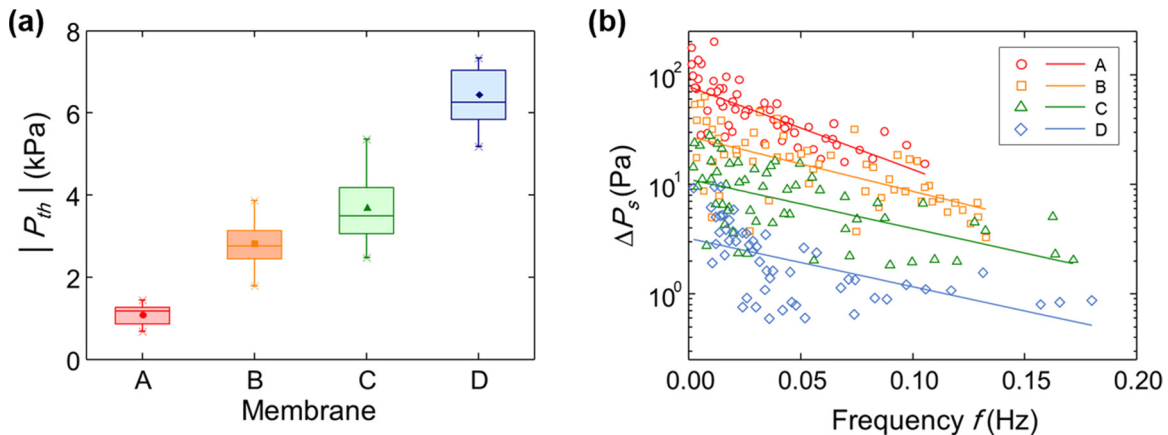


FIG. 4. Pressure variation characteristics according to the membranes. (a) Threshold pressure (P_{th}) required for the air to pass through each membrane. (b) Amplitude of pressure variations (ΔP_s) as a function of frequency f , analyzed by FFT of the pressure fluctuations during the type II air spreading. Sixty points were selected in the order of higher amplitude from the FFT results. Solid lines represent fitting curves of experimental data. As the membrane thickness increases, ΔP_s decreases and f is distributed in a broad region.

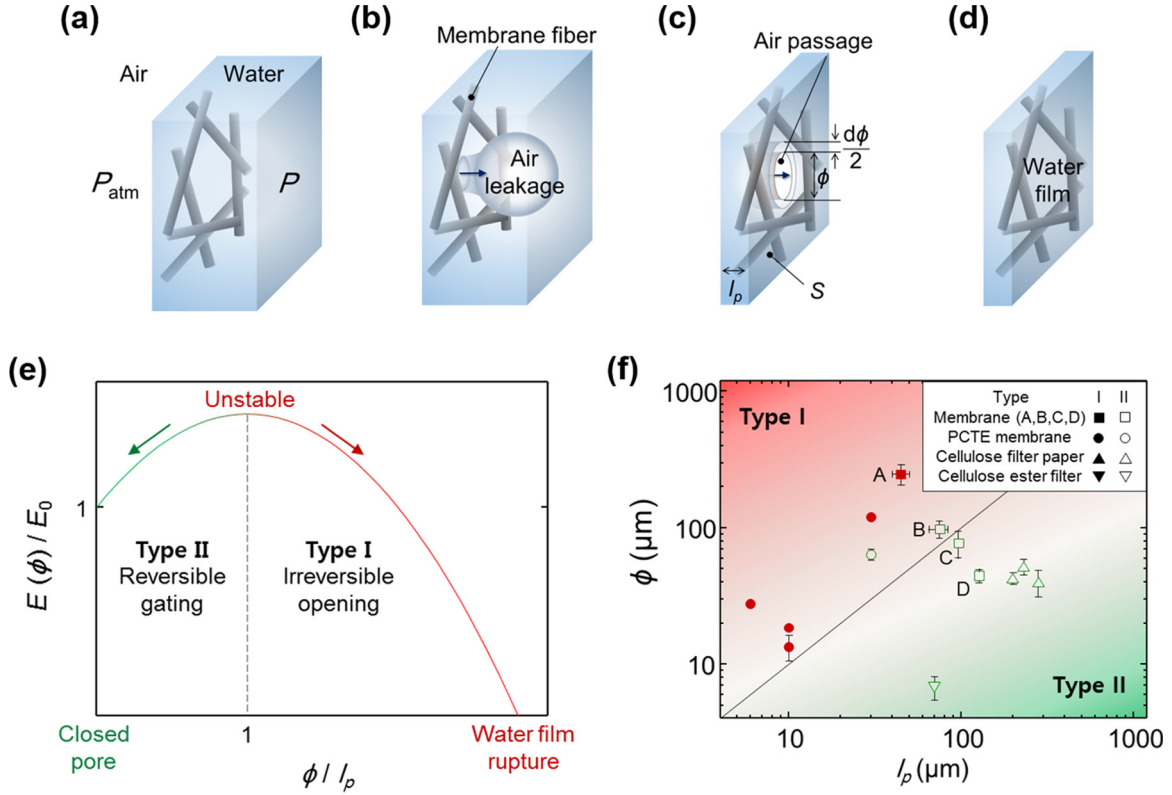


FIG. 5. Determination of the air spreading dynamics in a microscopic view. (a) The air-water meniscus is drawn across the membrane. (b) An air bubble leaks through an air passage formed between the membrane fibers. (c) The air keeps spreading through the opened pore. Air passage is simplified into a cylindrical shape whose diameter and length are denoted as ϕ and l_p , respectively. (d) Pore is closed by the water film captured by cellulose fibers. The spreading behaviors of type I do not show the close of the pore, while type II exhibits the behaviors of (c) and (d) repeatedly. Water is retained on the cellulose fibers of the membrane due to the hydrophilicity of cellulose during the whole process. (e) Interfacial energy $E(\phi)$ of the system according to ϕ/l_p . (f) Classification of air spreading behaviors into two types on the basis of the line of $\phi = l_p$.

expressed as

$$P_{th} = -\frac{4\gamma \cos \theta}{\phi}, \quad (1)$$

where ϕ is the diameter of air passage. Here, θ is the water contact angle on the membrane surface which is assumed to be 0° [8,11–14,26,27]. From Eq. (1), the diameters ϕ of the membranes A, B, C, and D are obtained as 248.5 ± 41.1 , 97.7 ± 13.17 , 77.4 ± 17.1 , and 44.6 ± 5.1 μm , respectively. A thick membrane is densely stacked with layers of cellulose fibers and has low porosity. As a result, thick membrane tends to have higher $|P_{th}|$ since the maximum size of air passage is likely to be small.

B. Two types of air spreading through the wetted cellulose membrane

After air leaks through the membrane, air spreading process exhibits two different dynamics, continuous spreading (type I) and discrete spreading (type II). The behaviors of type I can be observed during air spreading through the thinnest membrane. In this case, the air passage remains open and is unable to block the air flow [Fig. 5(c)]. Air keeps spreading across the membrane continuously. In type II, however, the air passage is closed by the residual water film, and air flow is sealed again [Fig. 5(d)]. In other

words, water film covering the membrane pores behaves as a gate for air penetration by repeating open and close. Meanwhile, the meniscus moves forward, repeating the cycle of advance and pause. The opening and closing cycles of air passages through wetted cellulose fibers for both types of air spreading were visualized in a microscopic view using x-ray imaging technique (videos S6, S7 and Fig. S5 [21]). In the biological perspective, water transport in plants would be interrupted seriously if embolism continuously spreads to adjacent xylem vessels like as type I. In contrast, it would have more chances to block the embolism spreading if the air passage through the pit membrane can be closed again like as type II.

We examined the criterion which determines the air spreading dynamics. Figure 5(c) shows air penetration through an air passage surrounded by cellulose fibers capturing water. The air passage is simplified into a cylindrical channel in which the length and diameter of the air passage are denoted as l_p and ϕ , respectively. Symbol S indicates the whole air-water interfacial area of the water film retained by the membrane. As the diameter of the air passage is enlarged by $d\phi$, the lateral surface area of the air passage increases as much as $\pi l_p d\phi$, while the planar surface area of the water film decreases by $\pi \phi d\phi$. The planar surface area of the water film is assumed to be large enough to neglect the increment in l_p . The

interfacial area S of the air-water interface of the microscopic system varies by

$$dS = \pi(-\phi + l_p)d\phi. \quad (2)$$

Therefore, the change of interfacial energy (dE) can be expressed as

$$dE = \gamma dS = \pi\gamma(-\phi + l_p)d\phi. \quad (3)$$

When we integrate Eq. (3) with respect to ϕ , interfacial energy E between the air and water becomes a function of ϕ as follows:

$$\frac{E(\phi)}{E_0} = \frac{\pi\gamma l_p^2}{2E_0} \left[-\left(\frac{\phi}{l_p}\right)^2 + 2\frac{\phi}{l_p} \right] + 1, \quad (4)$$

where E_0 is the interfacial energy in the initial state when the air passage is closed ($\phi = 0$).

As shown in Fig. 5(e), E is maximized (where $dE/d\phi = 0$) when

$$\phi = l_p, \quad (5)$$

and the system becomes energetically unstable. Since the system is favorable to lower the energy, ϕ will decrease until the air passage is completely closed with water for a given l_p when $\phi < l_p$. As P reaches P_{th} again, the air passage is reopened. Hence, the air passage can reversibly gate the air flow resulting discrete air spreading of type II. However, when $\phi > l_p$, air passage would energetically prefer to be enlarged with increasing ϕ . Water film is irreversibly ruptured and unable to be recovered. Therefore, air continuously spreads across the membrane showing the behavior of type I without blockage by the water film.

The criterion classifying the air spreading pattern into the types I (filled symbols) and II (hollow symbols) was compared with the experimental values of ϕ and l_p [Fig. 5(f)]. To support our hypothesis, the air spreading dynamics through various commercially available hydrophilic membranes, such as polycarbonate (PCTE) membranes, cellulose filter papers, and cellulose ester membranes, were also tested. Their specifications and SEM images are provided in the Supplemental Material (Fig. S6 and Table S1 [21]). The thickness of the membrane swollen with water was assumed as the length of air passage l_p . The diameter of the air passage ϕ of each membrane was evaluated by using Eq. (1). Straight line indicates the criterion of $\phi = l_p$. Therefore, the regions in the top left and bottom right are more likely to exhibit the behaviors of type I and type II, respectively. As the membrane thickness decreases, the experimental results were located closer to the top left, and vice versa. However, the experimental case of the membrane B that has shown the result of type II, is marked in the region of type I above the line of $\phi = l_p$. This could be resulted from that our simplified model of air passage underestimates l_p , without considering the complexity of air passage which increases with the membrane thickness.

In spite of the discrepancy between the experiment results and theoretical model, our expectation is still able to explain the different types of air spreading behavior according to the membrane thickness. Thin membrane is sparsely overlapped with less cellulose fibers forming large-size pores. In addition, air passage can be widened by the air penetration, because thin

membranes with low mechanical properties can be deformed or damaged. Therefore, ϕ is more likely to be larger than l_p , and thin membrane tends to show the type I air spreading to lower the interfacial energy of the system. On this basis, the water film captured by fibers of a thin membrane is hardly recovered once the air leaks through the wide air pathway. However, thick membranes are stacked with many fibers. Thus, ϕ of thick membrane is likely to be lower than l_p due to their narrow air pathways. The complex morphology of air pathway will also contribute to lengthen l_p . Therefore, thick membrane is energetically favorable to close their air passage by recovering the residual water films, even after the air leakage occurs.

C. Correlation between the type I of air spreading of type II and pressure variations

As P reaches P_{th} again, closed air pathway is reopened and air spreads across the membrane. Figure 6(a) shows temporal variations in air area A and negative pressure P measured at the downstream of the membrane during the n -th step ($t_n \leq t < t_{n+1}$) of air spreading with type II. Here, A has a recurrence relation of

$$A_{n+1} = A_n + s_{n+1}, \quad (6)$$

where s_n is the step size s during n th step. At $t = t_n$, the membrane pore is opened after P reaches the threshold pressure P_{th} . Afterwards, the area A rapidly increases from A_{n-1} to $A_n = A_{n-1} + s_n$. At the same time, the meniscus advances and P is released from P_{th} to $P_{th} + \Delta P_s$, where ΔP_s is the pressure increment during air seeding. As P increases above P_{th} , the pore is closed by the water film covering cellulose fibers, because the absolute pressure difference across the membrane decreases. The air stops spreading while maintaining A_n in constant. Simultaneously, P decreases, as the pore is closed. As P becomes the level of P_{th} at $t = t_{n+1}$, the pore is opened and the air-water meniscus moves forward again. The process illustrated in Figs. 5(c) and 5(d) and the meniscus movement which is directly correlated with pressure variation [Fig. 6(a)] are repeated in the case of type II. In addition, pressure difference across the cellulose membrane is consequently required for further air spreading in the manner of type II.

Thick membranes tend to have more chances to close their narrow, long, and complex air passages. Therefore, the pore is opened for a short time as the membrane thickness increases. The magnitudes of the step size s and the increment of pressure difference ΔP_s decrease together showing a positive correlation [Fig. 6(b)]. After the pore is closed, low ΔP_s indicates that P reaches P_{th} again in a short time and the pore is reopened. The reason is that the pressure decreasing rate is same for all experiments. Therefore, thick membrane repeats the cycle of breakage and recovery of the water film frequently with high f [Fig. 4(b)].

We investigated the dynamic characteristics of air spreading through cellulose membranes. A cellulose membrane blocks air penetration until the pressure difference across the membrane becomes a critical value. A thick membrane requires a high pressure difference for air penetration. After the air starts to leak through the membrane, the air spreading exhibits two types of behaviors. These behaviors are determined

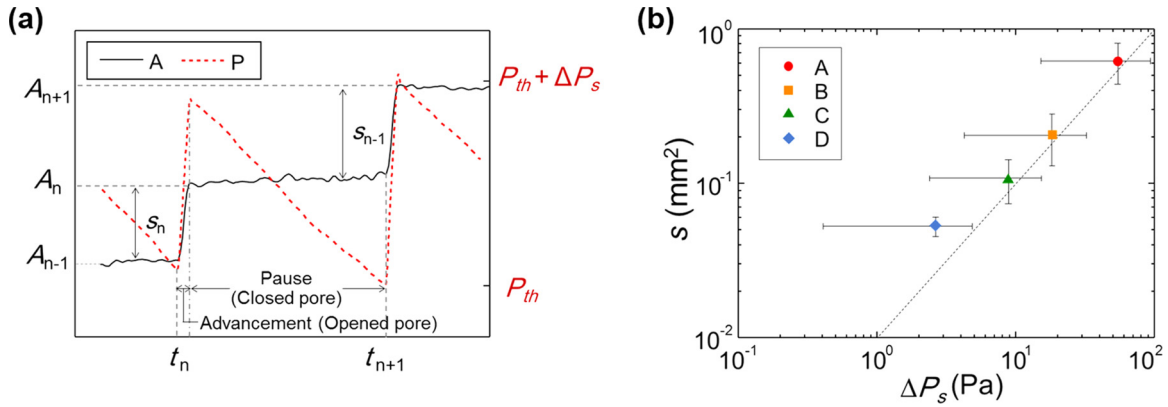


FIG. 6. Discrete air spreading through the membrane pore. (a) Relationship between temporal variations of the air area A and the pressure difference ΔP_s across the membrane during the n th step of advance and pause. (b) Proportional relationship between the step size s and the amplitude of pressure fluctuations ΔP_s .

by the relative magnitude of diameter and length of air passage in the way to lower the surface energy of the system. In the first type, which is only observed in the thinnest membrane, the pressure difference across the membrane approaches to near zero and the air continuously spreads along the channel. In the other type, pressure difference is persistently required for further air spreading. This type is attributed to the fact that cellulose membranes keep preventing air flow with water film serving as the gate of air flow by repeatedly opening and closing the pore. Air discretely spreads across a thick membrane with repeating the advance and pause frequently with small step size and pressure fluctuation.

D. Implication for the hydraulic functions of pit membranes

These results show the hydraulic functions of pit membranes as safety valves, which isolate embolized xylem conduits from well-functioning conduits. Pressure difference across the pit membrane must reach or exceed a certain threshold pressure for embolism spreading to adjacent conduits [6,8,11–14]. Thick pit membranes have higher resistance against the embolism spreading because they have small pore size, complex air pathway, and strong mechanical properties; as a result, they require relatively large air seeding pressure [6,12,28,29].

In addition, we suggest that the thickness of the pit membrane, which is directly related to the ratio between the length and size of the air passage, would be a crucial factor determining the spreading dynamics of embolism: continuous and discrete type. Discrete type of air spreading in this study implies another possible mechanism of limiting air flow across the pit membrane. Pit membranes woven with cellulose fibers can capture water film that works as a potential gate of embolism spreading. Even after air seeding, the residual water film at pit membranes is recovered and the spreading of embolism can be sealed again. In other words, the pressure difference across the pit membranes might be persistently required for further air seeding or spreading, which is accompanied with breaking of the water film. Moreover, the present results suggest that thick pit membranes tend to snap off small volume of gas bubbles with the water film infiltrated through the narrow air pathway, instead of generating continuous air stream during

the air seeding [30]. If the size of gas bubbles is smaller than the critical radius, they collapse immediately and are safe from expansion [30–32].

The mechanism by which water film reversibly blocks the embolism spreading facilitates growth of plants in dry season [33], high light intensity [34], and severe drought condition [35]. Plants have increased their resistance against cavitation by evolving thick pit membranes with small pores [12,13,29,36]. By contrast, thin pit membranes with high porosity are vulnerable to embolism, because they would be easily damaged by their stretching or deformation [6,28]. These thinner pit membranes are less likely to keep the pores closed with residual water film, and cavitation can be continuously spread to nearby xylem vessels.

The geometric scale of pit membranes in real plants is different from that of the experimental system used in this study. However, this study will be still effective to explain the hydraulic roles of wetted pit membranes. The pore size of pit membrane ranges from 10^1 to 10^2 nm [6]. The flow in submicron scale would not follow Hagen-Poiseuille equation since the continuum theory cannot be applied. It was verified that the flow in hydrophilic nanochannel increases due to water slippage on the channel surface as the channel diameter decreases below 100 nm [37]. In addition, the surface tension of air-water interface depends on the radius of curvature at the submicron scale [38,39]. However, the average diameter of pit membranes is in microscale [6]. Thus, the wetting property of water at the cellulose membrane is hardly affected and the proposed hypothesis of wetted pit membranes would be still effective. Even if the surface tension value varies, it is involved in the part of coefficient in Eq. (4). Thus, the surface tension value does not affect the criterion $\phi = l_p$ that can classify the air spreading dynamics into type I and type II. Therefore, the ratio of the membrane thickness and pore size would still be an important parameter that governs the embolism spreading dynamics.

V. CONCLUSION

Dynamics of the embolism spreading at a pit level have not been observed and still remain as a hypothesis [3,12]. We systematically investigated the hydrodynamic behaviors

of blocking and spreading of embolism at a pit level for the first time by using a biomimetic model system composed of a circular channel embedding a cellulose membrane. Dynamic characteristics of air flow and pressure variations were correlated with the membrane thickness, which reveals the two types of air spreading: continuous and discrete spreading. Our results suggest that the thickness of pit membrane, which is closely related with ratio between the length and size of air passage, would be a crucial factor that determines the type of embolism spreading. In addition, the water film captured by cellulose fibers might enable the reversible gating of the embolism spreading. Although the geometric scale of the present experimental system is different from that of real pit membranes, the present results would contribute to the understanding of the hydraulic functions of pit membranes retaining water film as safety valves against the risk of

cavitation. In addition, the biomimetic model system proposed in this study can be used to verify the hypothetical strategies of pit membranes for avoiding the risks of embolism.

ACKNOWLEDGMENTS

This work was supported by the National Research Foundation of Korea (NRF) grant funded by the Korean government (MSIP) (Grant No. 2017R1A2B3005415). The manuscript was written through contributions of all authors. J.P. and S.J.L. proposed the study. J.P. not only designed and carried out the experiments, but also finished the original draft. T.G. contributed to the analysis of experimental data and image processing. T.G. and J.R. reviewed and edited the draft critically. S.J.L. provided research funding and project administration.

-
- [1] K. H. Jensen, K. Berg-Sorensen, H. Bruus, N. M. Holbrook, J. Liesche, A. Schulz, M. A. Zwieniecki, and T. Bohr, *Rev. Mod. Phys.* **88**, 035007 (2016).
- [2] J. S. Sperry, *IAWA J.* **6**, 283 (1985).
- [3] M. D. Venturas, J. S. Sperry, and U. G. Hacke, *J. Integr. Plant Biol.* **59**, 356 (2017).
- [4] J. Pittermann, B. Choat, S. Jansen, S. A. Stuart, L. Lynn, and T. E. Dawson, *Plant Physiol.* **153**, 1919 (2010).
- [5] H. Ooeda, I. Terashima, and H. Taneda, *Plant Cell Physiol.* **58**, 354 (2017).
- [6] S. Jansen, B. Choat, and A. Pletsers, *Am. J. Bot.* **96**, 409 (2009).
- [7] B. Choat, M. Ball, J. Luly, and J. Holtum, *Plant Physiol.* **131**, 41 (2003).
- [8] B. Choat, A. R. Cobb, and S. Jansen, *New Phytol.* **177**, 608 (2008).
- [9] D. Klemm, B. Heublein, H. P. Fink, and A. Bohn, *Angew. Chem. Int. Ed.* **44**, 3358 (2005).
- [10] M. T. Tyree and M. H. Zimmermann, *Xylem Structure and the Ascent of Sap* (Springer, Berlin, 2002).
- [11] J. Pittermann, J. S. Sperry, U. G. Hacke, J. K. Wheeler, and E. H. Sikkema, *Science* **310**, 1924 (2005).
- [12] S. Li, F. Lens, S. Espino, Z. Karimi, M. Klepsch, H. J. Schenk, M. Schmitt, B. Schuldt, and S. Jansen, *IAWA J.* **37**, 152 (2016).
- [13] L. Plavcova, S. Jansen, M. Klepsch, and U. G. Hacke, *Front. Plant Sci.* **4**, 453 (2013).
- [14] M. Capron, P. Tordjeman, F. Charru, E. Badel, and H. Cochard, *Phys. Rev. E* **89**, 033019 (2014).
- [15] A. Tixier, S. Herbette, S. Jansen, M. Capron, P. Tordjeman, H. Cochard, and E. Badel, *Ann. Bot.* **114**, 325 (2014).
- [16] J. S. Sperry and U. G. Hacke, *Am. J. Bot.* **91**, 369 (2004).
- [17] S. J. Lee, J. Park, and J. Ryu, *Front. Plant Sci.* **9**, 1931 (2018).
- [18] R. G. Mannino, D. R. Myers, B. Ahn, Y. Wang, M. Rollins, H. Gole, A. S. Lin, R. E. Guldberg, D. P. Giddens, L. H. Timmins, and W. A. Lam, *Sci. Rep.* **5**, 12401 (2015).
- [19] C. T. Rueden, J. Schindelin, M. C. Hiner, B. E. DeZonia, A. E. Walter, E. T. Arena, and K. W. Eliceiri, *BMC Bioinformatics* **18**, 529 (2017).
- [20] N. A. Hotaling, K. Bharti, H. Kriel, and C. G. Simon, Jr., *Biomaterials* **61**, 327 (2015).
- [21] See Supplemental Material at <http://link.aps.org/supplemental/10.1103/PhysRevE.100.032409> for the SEM images of the cellulose membranes used in this study (Fig. S1), representative imbibition behaviors of water droplet through the membrane D (Fig. S2), fourier transform infrared (FTIR) spectra of the membranes used in this study (Fig. S3), two types of bubble spreading behaviors through the membranes (Fig. S4), and visualization of the behaviors of air passage (Fig. S5), SEM images of hydrophilic membranes tested in Fig. 5(f) (Fig. S6), specifications of the hydrophilic membranes (Table S1), spreading of air through the cellulose membranes (Videos S1–S5), air spreading dynamics at the air passage (Videos S6 and S7).
- [22] M. F. Rosa, E. S. Medeiros, J. A. Malmonge, K. S. Gregorski, D. F. Wood, L. H. C. Mattoso, G. Glenn, W. J. Orts, and S. H. Imam, *Carbohydr. Polym.* **81**, 83 (2010).
- [23] M. Poletto, V. Pistor, M. Zeni, and A. J. Zattera, *Polym. Degrad. Stabil.* **96**, 679 (2011).
- [24] D. Ciolacu, F. Ciolacu, and V. I. Popa, *Cell. Chem. Technol.* **45**, 13 (2011).
- [25] S. Chang, J. Seo, S. Hong, D.-G. Lee, and W. Kim, *J. Fluid Mech.* **845**, 36 (2018).
- [26] A. D. Stroock, V. V. Pagay, M. A. Zwieniecki, and N. M. Holbrook, *Ann. Rev. Fluid Mech.* **46**, 615 (2014).
- [27] M. A. Zwieniecki and N. M. Holbrook, *Plant Physiol.* **123**, 1015 (2000).
- [28] F. Lens, A. Tixier, H. Cochard, J. S. Sperry, S. Jansen, and S. Herbette, *Curr. Opin. Plant Biol.* **16**, 287 (2013).
- [29] F. Lens, J. S. Sperry, M. A. Christman, B. Choat, D. Rabaey, and S. Jansen, *New Phytol.* **190**, 709 (2011).
- [30] H. J. Schenk, K. Steppe, and S. Jansen, *Trends Plant Sci.* **20**, 199 (2015).
- [31] W. Konrad, G. Katul, A. Roth-Nebelsick, and K. H. Jensen, *Tree Physiol.* **39**, 243 (2019).
- [32] W. Konrad and A. Roth-Nebelsick, *J. Theor. Biol.* **224**, 43 (2003).
- [33] N. Schmitz, G. Koch, U. Schmitt, H. Beeckman, and N. Koedam, *Microsc. Microanal. M* **14**, 387 (2008).

- [34] L. Plavcová, U. G. Hacke, and J. S. Sperry, *Plant Cell Environ.* **34**, 501 (2011).
- [35] I. M. Aref, A. I. Ahmed, P. R. Khan, H. A. El-Atta, and M. Iqbal, *Trees* **27**, 959 (2013).
- [36] A. Scholz, D. Rabaey, A. Stein, H. Cochard, E. Smets, and S. Jansen, *Tree Physiol.* **33**, 684 (2013).
- [37] K. P. Lee, H. Leese, and D. Mattia, *Nanoscale* **4**, 2621 (2012).
- [38] S. Kwon, B. Kim, S. An, W. Lee, H. Kwak, and W. Jhe, *Sci. Rep.* **8**, 8462 (2018).
- [39] S. Burian, M. Isaiev, K. Termentzidis, V. Sysoev, and L. Bulavin, *Phys. Rev. E* **95**, 062801 (2017).